# Godunov-type methods for two-component magnetohydrodynamic equations

## K. MURAWSKI[1*] and T. TANAKA[2]

[1] Faculty of Physics, Mathematics and Informatics, UMCS, 10 Radziszewskiego St., 20-031 Lublin, Poland
[2] Department of Earth and Planetary Sciences, Faculty of Sciences, Kyushu University,
6-10-1 Hakozaki, Higashi-ku, Fukuoka 812-8581, Japan

**Abstract.** This paper is concerned with a numerical solutions of two-component magnetohydrodynamic equations. While a hyperbolic system of wave equations admits a shock solution as a result of the selenoidality condition the MHD equations are not strictly hyperbolic. As a consequence of that these equations require special numerical treatment. An application of a resulting numerical code to a problem of solar wind interaction with the ionosphere of the planet Venus is presented.

**Key words:** two-component magnetohydrodynamic equations, Godunov-type methods.

## 1. Introduction

In the magnetohydrodynamic (MHD) model, the plasma is described by fluid equations and Maxwell's equations e.g., [1]. Although these equations consist of the simplest self-consistent model describing macroscopic properties of plasma, the full nonlinear MHD equations are so complex that usually significant simplifications are required to yield analytically tractable problems. Therefore, many solutions of MHD equations require numerical treatment. Finite-volume methods are one of several different techniques available to solve these equations. These methods are simple to implement, easily adaptable to complex geometries, and well suited to handle nonlinear terms.

Like solutions of nonlinear hyperbolic equations solutions of MHD equations exhibit the tendency to form steep spatial profiles (e.g., shock and contact waves) which are difficult for numerical treatment. The implementation of standard numerical schemes of second-order accuracy (e.g., the Lax-Wendroff method) results in dispersive oscillations which pollute the solution [2]. Lower-order schemes e.g., [3] are usually free of such oscillations, but they are so dissipative as they wash out much of the details at steep plasma profiles. Therefore, there is a need to develop more advanced schemes which would adequately represent such steep spatial profiles. These schemes belong to a family of Godunov-type methods which are particularly designed to capture well shocks.

Is is noteworthy here that extending a well performing numerical method which solves hydrodynamic (HD) equations to a MHD code is not a straightforward task since various kinds of singularities are present in the MHD equations. As a result of this intrinsic complexity of the MHD equations, the development of numerical techniques to solve these equations has been slower than for hydrodynamics. For decades many numerical schemes used artificial viscosity to represent adequately shocks and contact waves e.g., [4]. Although

these schemes performed successfully in numerical modeling of astrophysical system e.g., [5], the past experience with Gudunov-type methods revealed latter to be superior in many applications [6]. It is therefore natural to extend such schemes to solve MHD conservation equations. However, there are two major difficulties associated with the numerical solution of the MHD equations as compared to their HD counterparts [7]: (a) MHD equations represent new families of waves and admit a variety of exotic wave structures such as compound waves of either fast or slow magnetoacoustic waves. This has a considerable impact on a performance of the algorithms which are required to provide the stable and accurate capture of this entire range of such structures e.g., [8]. Roe and Balsara [7] list the six cases that can potentially cause trouble; (b) MHD equations contain the magnetic field which has to satisfy the divergence-free constraint, $\nabla \cdot \mathbf{B} = \mathbf{0}$. A local nonzero divergence of magnetic field results in the existence of magnetic monopoles within the numerical cell, which leads to non-conservation of the magnetic flux across its surface. Accumulation of the numerical errors associated with evolving the magnetic field components can lead to violation of this constraint, leading to an artificial force parallel to the magnetic field.

Despite the above mentioned problems many numerical schemes were developed for the MHD equations. These schemes reveal either conservative or non-conservative properties of these equations and they are briefly described in this paper as well as their excellent performance in numerical modeling of the solar wind interaction with the ionosphere of the planet Venus.

## 2. Two-component MHD equations

Astrophysical plasma very often consists of multi-component species [9]. In this case, MHD equations should be extended to multi-component MHD equations. Despite this extension,

MHD equations can still be written in the conservation form. Below we consider the simplest conceivable case of two plasma species which dynamics is described by two-component MHD equations which were originally derived in [9]. However, [9] concentrates on a development of a physical model while in this paper we make emphasis on numerical issues associated with this model.

We specify the total density, $\varrho$, as

$$\varrho = \varrho_1 + \varrho_2\,, \qquad (1)$$

where two species of plasma are denoted by $\varrho_1$ and $\varrho_2$, respectively. We express magnetic field $\mathbf{B}$ as

$$\mathbf{B} = \mathbf{B}_0 + \mathbf{B}_1, \qquad (2)$$

where the background magnetic field, $\mathbf{B}_0$, is assumed to be potential.

We introduce now a vector state $\mathbf{u}_1$ as

$$\begin{aligned} \mathbf{u}_1 &= (\varrho, \mathbf{m}, \mathbf{B}_1, E_1, \varrho_2)^T \\ &= (\varrho, m_x, m_y, m_z, B_x - B_{0x}, B_y - B_{0y}, B_z - B_{0z}, \\ &\quad E - (\mathbf{B}_1 \cdot \mathbf{B}_0)/\mu - B_0^2/(2\mu), \varrho_2)^T, \end{aligned} \qquad (3)$$

and rotate the dependent variables

$$\begin{aligned} \mathbf{u}_n &= \mathbf{Tu} = (\varrho, \mathbf{m}_n, \mathbf{B}_n, E, \varrho_2)^T \\ &= (\varrho, m_n, m_{t1}, m_{t2}, B_n, B_{t1}, B_{t2}, E, \varrho_2)^T. \end{aligned} \qquad (4)$$

Then, we can write the equation for $\mathbf{u}_1$ as [9]

$$\frac{\partial}{\partial t} \int \mathbf{u}_1 dv + \int \mathbf{T}^{-1} \mathbf{F}(\mathbf{u}_{1n}, \mathbf{B}_{0n}) ds = \int \mathbf{S} dv, \qquad (5)$$

where $\mathbf{S}$ is the source term, $dv$ and $ds$ are the volume and surface elements of the control volume and $\mathbf{T}$ is a matrix which rotates the $x$-axis to the direction of a unit vector $\mathbf{n}$ normal to the surface of the control volume. The flux function, $\mathbf{F}$, in the normalized form is written as

$$\mathbf{F} = \begin{bmatrix} m_n \\ p + \frac{m_n m_n}{\varrho} + \frac{B^2}{2\mu} - \frac{1}{\mu} B_n B_n - \frac{B_0^2}{2\mu} + \frac{1}{\mu} B_{0n} B_{0n} \\ \frac{m_{t1} m_n}{\varrho} - \frac{1}{\mu} B_{t1} B_n + \frac{1}{\mu} B_{0t1} B_{0n} \\ \frac{m_{t2} m_n}{\varrho} - \frac{1}{\mu} B_{t2} B_n + \frac{1}{\mu} B_{0t2} B_{0n} \\ 0 \\ \frac{m_n}{\varrho} B_{t1} - \frac{m_{t1}}{\varrho} B_n \\ \frac{m_n}{\varrho} B_{t2} - \frac{m_{t2}}{\varrho} B_n \\ \frac{m_n}{\varrho}(E_1 + \frac{B_1^2}{2\mu} + p) - \frac{B_{1n}}{\mu} \\ \times(\frac{m_n}{\varrho} B_{1n} + \frac{m_{t1}}{\varrho} B_{1t1} + \frac{m_{t2}}{\varrho} B_{1t2}) \\ + \frac{B_{1t1}}{\mu}(\frac{m_n}{\varrho} B_{0t1} - \frac{m_{t1}}{\varrho} B_{0n}) \\ + \frac{B_{1t2}}{\mu}(\frac{m_n}{\varrho} B_{0t2} - \frac{m_{t2}}{\varrho} B_{0n}) \\ \frac{\varrho_2}{\varrho} m_n \end{bmatrix}. \qquad (6)$$

**2.1. Eigenvalues and eigenvectors of the Jacobian.** For the Jacobian matrix of 9-th component flux function, eigenvalues $\lambda^m$, $m = 1, \ldots, 9$ are

$$\lambda^1 = m'_n, \qquad (7)$$

$$\lambda^{2,3} = m'_n \pm |B'_n|, \qquad (8)$$

$$\lambda^{4,5} = m'_n \pm c_+, \qquad (9)$$

$$\lambda^{6,7} = m'_n \pm c_-, \qquad (10)$$

$$\lambda^8 = 0, \qquad (11)$$

$$\lambda^9 = m'_n, \qquad (12)$$

with the notation

$$\begin{aligned} \mathbf{u}'_n &= (\varrho, \mathbf{m}'_n, \mathbf{B}'_n, E, \varrho_2)^T \\ &= (\varrho, m_n/\varrho, m_{t1}/\varrho, m_{t2}/\varrho, B_n/\sqrt{\mu\varrho}, B_{t1}/\sqrt{\mu\varrho}, \\ &\quad B_{t2}/\sqrt{\mu\varrho}, E, \varrho_2)^T. \end{aligned}$$

Here, variables with $'$ have a dimension of velocity and $|B'_n|$, $c_+$ and $c_-$ correspond to Alfvén, fast and slow speeds, respectively. The eigenvectors $\mathbf{r}_m$ which correspond to $\lambda^m$ are

$$\mathbf{r}^1 = \begin{bmatrix} 1 \\ m'_n \\ m'_{t1} \\ m'_{t2} \\ 0 \\ 0 \\ 0 \\ m'^2/2 \\ 0 \end{bmatrix}, \qquad (13)$$

$$\mathbf{r}^{2,3} = \begin{bmatrix} 0 \\ 0 \\ \mp B''_{t2} \cdot sgn(B'_n) \\ \pm B''_{t1} \cdot sgn(B_n) \\ 0 \\ B''_{t2} \sqrt{\frac{\mu}{\varrho}} \\ -B''_{t1} \sqrt{\frac{\mu}{\varrho}} \\ \mp(B''_{t2} m'_{t1} - B''_{t1} m'_{t2}) \cdot sgn(B'_n) \\ +(B''_{t2} B'_{1\,t1} - B''_{t1} B'_{1\,t2}) \\ 0 \end{bmatrix}, \qquad (14)$$

$$\mathbf{r}^{4,5} = \begin{bmatrix} a_f \\ a_f(m'_n \pm c_+) \\ a_f m'_{t1} \mp a_s B''_{t1} c_+ B'_n \\ a_f m'_{t2} \mp a_s B''_{t2} c_+ B'_n \\ 0 \\ a_s B''_{t1} c_+^2 \sqrt{\frac{\mu}{\varrho}} \\ a_s B''_{t2} c_+^2 \sqrt{\frac{\mu}{\varrho}} \\ a_f \cdot 0.5 \cdot m'^2 + a_f c_+^2/(\gamma-1) \pm a_f c_+ m'_n \\ \mp a_s c_+ (B''_{t1} m'_{t1} + B''_{t2} m'_{t2}) B'_n \\ + a_f(-1)/(\gamma-1)(c_+^2 - c_0) \\ + a_f(c_+^2 - c_0)(B''_{t1} B'_{1t1} + B''_{t2} B'_{1t2}) \\ /(B''^2_{t1} + B''^2_{t2}) \\ a_f \varrho_2/\varrho \end{bmatrix}, \quad (15)$$

$$\mathbf{r}^{6,7} = \begin{bmatrix} a_s \\ a_s(m'_n \pm c_-) \\ a_s m'_{t1} \pm a_f B''_{t1} \sqrt{c_0}/c_+ \cdot sgn(B'_n) \\ a_s m'_{t2} \pm a_f B''_{t2} \sqrt{c_0}/c_+ \cdot sgn(B'_n) \\ 0 \\ -a_f B''_{t1} \sqrt{\frac{\mu}{\varrho}} c_0/c_+^2 \\ -a_f B''_{t2} \sqrt{\frac{\mu}{\varrho}} c_0/c_+^2 \\ a_s \cdot 0.5 \cdot m'^2 + a_s c_-^2/(\gamma-1) \pm a_s c_- m'_n \\ \pm a_f(B''_{t1} m'_{t1} + B''_{t2} m'_{t2}) \\ \times \sqrt{c_0}/c_+ \cdot sgn(B'_n) + a_s(-1)/(\gamma-1)(c_-^2 - c_0) \\ + a_s(c_-^2 - c_0)(B''_{t1} B'_{1t1} + B''_{t2} B''_{1t2}) \\ /(B''^2_{t1} + B''^2_{t2}) \\ a_s \varrho_2/\varrho \end{bmatrix},$$
$$(16)$$

$$\mathbf{r}^8 = \begin{bmatrix} 0 \\ 0 \\ 0 \\ 0 \\ 1 \\ 0 \\ 0 \\ 0 \\ 0 \end{bmatrix}, \quad \mathbf{r}^9 = \begin{bmatrix} 1 \\ m'_n \\ m'_{t1} \\ m'_{t2} \\ 0 \\ 0 \\ 0 \\ 0.5 \cdot m'^2 \\ 1 \end{bmatrix}, \quad (17)$$

where

$$B''_{t1} = (B'_{t1} + \epsilon)/(B'^2_{t1} + B'^2_{t2} + 2\epsilon^2)^{1/2}, \quad (18)$$

$$B''_{t2} = (B'_{t2} + \epsilon)/(B'^2_{t1} + B'^2_{t2} + 2\epsilon^2)^{1/2}, \quad (19)$$

$$a_f = (c_+^2 - B'^2_n)^{1/2}/(c_+^2 - c_-^2)^{1/2}, \quad (20)$$

$$a_s = (c_+^2 - c_0)^{1/2}/(c_+^2 - c_-^2)^{1/2} c_+. \quad (21)$$

The symbol $\epsilon$ is a small number and $c_0$ is the sound speed. Then the upwind numerical flux $\underline{\mathbf{F}}_{ij}$ at the interface of control volumes i and j can be written as

$$\underline{\mathbf{F}}_{ij} = \frac{1}{2}[\mathbf{F}(\mathbf{u}_{1nj}, \mathbf{B}_{0nj}) + \mathbf{F}(\mathbf{u}_{1ni}, \mathbf{B}_{0ni})$$
$$- \mathbf{R}_{ij} \mid \mathbf{\Lambda}_{ij} \mid \mathbf{R}_{ij}^{-1}(\mathbf{u}_{1nj} - \mathbf{u}_{1ni})], \quad (22)$$

where the eigenvector matrix $\mathbf{R}_{ij}$ and the eigenvalue matrix $\mathbf{\Lambda}_{ij}$ are calculated from the symmetric average of $\mathbf{u}_{1nj}$ and $\mathbf{u}_{1ni}$. To get a higher-order accuracy, the MUSCL scheme is used with indices $i$ and $j$ being replaced by $r$ and $l$, suffixes which indicate variables just on the left and right sides of the interface [10].

## 3. Implementation of the 9-th wave Riemann solver to the problem of solar wind interaction with Venus

The planet Venus has been the subject of intense investigation since Mariner 2 flew by the planet in the Fall 1962. Observations of Venus by orbital missions have led to a significant improvement of our knowledge about the upper atmosphere and ionosphere of Venus and their interaction with the solar wind. Since the internal magnetic field of Venus is negligibly small or even nonexistent, the solar wind interaction with Venus differs from their terrestrial counterparts. This lack of magnetic field allows the solar wind to make direct contact with the ionosphere of the planet.

Pioneer Venus Orbiter (PVO) as well as other spacecraft observations revealed that the solar wind interaction with Venus leads to a highly structured plasma [11]. As a result of supersonic and superalfvénic solar wind flow, a *bow shock* forms upstream of the planet. The shock serves to slow, heat, and also assists in deflecting the solar wind. The shock which for average solar wind conditions is a standing fast magnetoacoustic wave departs itself from the obstacle so that the plasma that crossed the shock can flow around the planet. The size of the bow shock depends on the solar wind Mach numbers, solar wind dynamic pressure, as well as on the shape and the size of the ionosphere [12]. Apparent asymmetries in the shock shape result from the oblique to the solar wind flow interplanetary magnetic field (IMF) [13].

Downstream of the bow shock, there exists a sharp gradient in the electron density known as *ionopause*. This is a region which separates the shocked and magnetized solar wind plasma from the thermal ionospheric plasma. The ionopause forms at the altitude above the surface of Venus where the ionospheric gas pressure is approximately balanced by the incident pressure in the overlaying magnetic barrier. The ionopause was observed to be typically located at about 300 km in the subsolar region and about 1000 km near the terminator [11]. It is generally accepted that the height of the terminator ionopause affects the transport of ionospheric plasma to the nightside. On occasion when the solar wind dynamic pressure is high enough to substantially lower the terminator ionopause altitude, the nightside ionosphere observed by PVO is found to be highly depleted [14]. This phenomenon is called the disappearing ionosphere.

The region between the bow shock and the ionopause is referred to as the *magnetosheath* [11]. The magnetosheath by itself contains a region (close to the ionopause) of enhanced magnetic pressure referred to as the *magnetic barrier* [12].

It is well known that Venus has a dayside exosphere which is dominated by oxygen at altitudes above 400 km from the planetary surface. The *ionosphere* is a partially-ionized component of exosphere above about 140 km from the surface of Venus Fig. 1. This region contains electrons and various ion species such as $O^+$, $H^+$, $O_2^+$, $CO_2^+$, and others. The ionosphere is approximately in photochemical equilibrium below an altitude of about 200 km at Venus for all ions. Above 200 km, $O^+$ becomes the major ion in this region. The principal ionization source on the dayside is provided by solar photoionization of thermospheric gases like $O$ by solar extreme ultraviolet (EUV) radiation, although other ionization processes such as impact ionization and charge exchange may also contribute in a major way. On the nightside, solar photoionization does not contribute directly to the ionization, and the maintenance of the nightside ionosphere requires ion transport from the dayside through the terminator. The nightward ion flow is driven primarily by the large pressure gradient at the terminator. The ion flow generally increases with solar zenith angle (SZA), reaching values larger than 7 km/s downstream of the terminator [15]. Ion-neutral chemical reactions and electron-ion charge exchange are both important processes in the lower ionosphere.
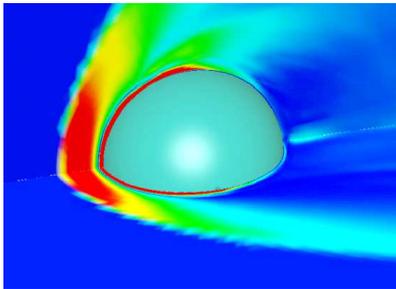


Fig. 1. Pressure distribution around Venus. The equatorial and meridian planes are horizontaland and vertical, respectively

The observations of the nightside ionosphere provided an evidence that the ionospheric plasma is highly structured and dynamic, often exhibiting large-scale structures which are called *tail rays*. The ionosphere has a tendency to form a central tail ray, often with rays on either side, to the north and south. The rays have dimensions of the order of $1-3 \times 10^3$ km, decreasing in width at higher altitudes [15]. Although the downstream extent of these structures is not measured since spacecraft orbits crossed them almost horizontally, it is supposed that they must extend tailward at least few thousand kilometers downstream.

In the nightside ionosphere, there are also regions of mass density depletions referred to as *ionospheric holes*. The density in these holes is lower than in the surrounding ionosphere by up to two orders of magnitude. The plasma in the holes differs from that found in their surrounding; $H^+$ becomes a major ion in the holes, while $O^+$ is the major ion outside.

These holes are associated with a strong magnetic field which points tailward.

Most recent numerical simulations of the three-dimensional interaction between the solar wind and Venus largely improved our understanding of the large scale physical processes [5, 9, 16]. In particular, Murawski and Steinolfson [5] included mass loading due to photoionization of the oxygen atoms and show that the solar wind is decelerated by the mass loading and the bow shock is pushed farther outward from the planet. However, this model was developed for the case when the IMF is parallel to the solar wind flow, simplifying the geometry to two dimensions. This model was extended to three dimensions by Murawski and Steinolfson [5] and the case of the IMF perpendicular to the solar wind flow was considered. In another model, solar wind interaction with the ionosphere of Venus was numerically simulated in the framework of two-component, three-dimensional MHD model by Tanaka and Murawski [9]. This model is briefly described here. The effect of decreased ionospheric pressure which occurs under the condition of high speed solar wind or low solar extreme ultraviolet (EUV) flux, was discussed by Tanaka [16]. The results of numerical simulations showed that the IMF penetrates from the magnetosheath to the dayside ionosphere so as to increase the ionospheric total pressure.

It is a purpose of this subsection to demonstrate that the basic features of the solar wind interaction with the ionosphere of Venus can be reproduced by applying a two-component MHD model which was developed by Tanaka and Murawski [9] and Tanaka [16]. This subsection is organized as follows. Numerical model of the dynamics of the solar wind and ionospheric plasma is reviewed in Subsec. 3.1. Numerically obtained results and discussion are presented in the following section. This subsection closes with some concluding remarks.

**3.1. Numerical model.** We describe the neutral atmosphere of Venus as a region which consists of the oxygen atoms and of the carbon dioxide molecules which both are stratified gravitationally. Their number densities at the lower boundary of the atmosphere are $10^{10}$ 1/cm$^3$ and $5 \cdot 10^{10}$ 1/cm$^3$, respectively. The peak number densities occur at altitude 140 km above the planetary surface, in agreement with the PVO observations [17]. The ionosphere is approximately in photochemical equilibrium at lower altitudes. $O^+$ ions are produced primarily by the solar EUV incident on the neutral atmosphere, $O + h\nu \rightarrow O^+$, and by charge exchange with $CO_2^+$ ions, $CO_2^+ + O \rightarrow O^+ + CO_2$. These chemical reactions occur with the production rates $q_1 = 10^{-10}$ 1/(cm$^3$ s) and $q_2 = 10^{-10}$ 1/(cm$^3$ s), respectively. The density of $CO_2^+$ ions is calculated from the photo-chemical equilibrium. $O^+$ ions experience some losses during their charge exchange with molecules of the carbon dioxide, viz., $O^+ + CO_2 \rightarrow CO + O_2^+$. The loss rate for $O^+$ ions is $L_1 = 9.4 \cdot 10^{-10}$ 1/(cm$^3$ s). $CO_2^+$ ions are produced by the photoionization of the carbon dioxide molecules, $CO_2 + h\nu \rightarrow CO_2^+$, and they experience charge losses during a chemical reaction with the oxygen atoms, viz., $CO_2^+ + O \rightarrow O_2^+ + CO$. The loss rate for $CO_2^+$ ions is $L_2 = 1.64 \cdot 10^{-10}$ 1/(cm$^3$ s).

We assume that the solar wind plasma consists of $H^+$ ions which flow with the same velocity as $O^+$ ions. The set of equations used for a description of the solar wind interaction with Venus is that of two-component, ideal MHD that includes mass production and loss terms in the mass continuity equation, and aeronomical collision and gravity terms in the momentum equation. We solve the set of two-component MHD equations, given by Eq. (5). The source term $\mathbf{S}$ in these equations depends on ion production due to photoionization and ion-neutral chemistry, $q_1$, $q_2$, as well as on losses due to ion-neutral reactions, $L_1$, $L_2$ ($H^+$ ion-electron recombination is neglected in this model), viz.,

$$\mathbf{S} = (q_1 + q_2 - L_1 - L_2, -\nu\mathbf{m} - \varrho\mathbf{g}, 0, 0, 0,$$

$$-\frac{\mathbf{m}}{\varrho} \cdot (\nu\mathbf{m} + \varrho\mathbf{g}) + \frac{T_q}{\gamma - 1}(q_1 + q_2) \qquad (23)$$

$$-\frac{T_L}{\gamma - 1}(L_1 + L_2), q_2 - L_2)^T.$$

In the above formulas, $\nu$ is the ion-neutral drag collision frequency, $\gamma = 5/3$ is the ratio of specific heats, $T_q = 10^3$ K is a production temperature of photoions and $T_L$ is a loss temperature due to a chemical reaction of the $O^+$ ions with the carbon dioxide. The other terms are self-explanatory.

We set the initial magnetic field perpendicular to the solar wind flow, while the IMF is typically oriented about $42°$ from the Sun-Venus line in the proper sense for an Archimedean spiral. As the perpendicular magnetic field case is simpler than the oblique field case, the present simulations will provide an insight into the more complex case. Consequently, the perpendicular magnetic field case seems to be motivated.

Equation (5) is solved in all three spatial dimensions of a spherical $r$, $\theta$, $\phi$ coordinate system by adopting a finite-volume method which uses a TVD scheme which was already successfully applied for a single-component plasma [10]. For Eq. (5), the size of the Jacobian matrix is $9 \times 9$. The eigenvalue problem for this Jacobian consists of two Alfvén, two fast, two slow, and two entropy waves. Consequently, there is one more entropy wave in comparison to the eigen-waves of the Jacobian of the one-component MHD equations. Details of the present approach can be found elsewhere [9].

The inner and outer boundaries of the simulation region are set at about $1 R_p$ and $10 R_p$, respectively. Here $R_p = 6053$ km + 140 km is the planetary radius. While the inflow boundary conditions are maintained on the dayside of the outer boundary, the zero-gradient boundary conditions are adopted on the downstream side. Near the inner boundary, the ion-neutral collision and ion chemical processes become dominant. Therefore, an ion chemical equilibrium and zero plasma velocity conditions are adopted at the inner boundary. The ion temperature is fixed and held constant at the inner boundary throughout the simulation process.

The numerical region was covered by $88 \times 80 \times 86$ grid points along $r \times \theta \times \phi$ directions, which lead to angular resolution of $\Delta\theta = 4.5°$ and $\Delta\phi \simeq 4°$. The radial grid was chosen nonuniform with a finest grid of $0.00025 R_p$ at the inner boundary of the simulation region. The coarsest grid of $0.33 R_p$ was set at the outer boundary.

A typical computation begins with the introduction of the desired solar wind values in the dayside within the numerical box. The numerical solution then continues until the interaction process achieves an approximate steady state.

**3.2. Numerical results and discussion.** We report here only some of the results from our simulations. More details can be found in Tanaka and Murawski [9]. We present all numerical results for the following solar wind parameters: proton density $n_e = 14$ cm$^{-3}$, temperature $T = 10^5$ °K, sound speed 61 km/s, solar wind speed 311 km/s which gives sonic Mach number 5.1, the plasma $\beta = 0.6$, and the magnetic field strength 15 nT. These parameters correspond to the maximum of solar activity [18].
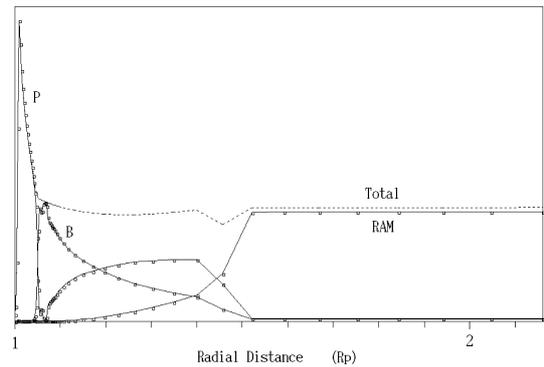


Fig. 2. The distribution of the gas pressure $p$, the magnetic pressure $p_B$, and the dynamic pressure $\varrho V^2$ along the Sun-Venus line on the subsolar side. The horizontal axis shows the radial distance normalized to the planet radius $R_p$ and the vertical axis shows relative pressure values. Note the bow shock at the distance $0.45 R_p$, the ionopause at the altitude about $0.04 R_p$, and the magnetic barrier which corresponds to the maximum of the magnetic pressure

Figure 2 shows the pressure profiles along the Sun-Venus line. In the upstream solar wind, kinetic pressure $\varrho V^2$ dominates gas pressure $p$ and magnetic pressure $B^2/(2\mu)$. At the bow shock, kinetic energy of the solar wind is converted into thermal energy. As a consequence of that, the gas pressure dominates over the kinetic pressure downstream the bow shock. The distance between the bow shock and the planetary surface is about $0.45 R_p \simeq 2700$ km, where $R_p \simeq 6053$ km is the radius of Venus (Fig. 2). With a distance closer to the planetary surface, the magnetic pressure accommodates itself as a result of competitive ionospheric gas pressure, while at the same time gas pressure decreases. This behavior is a consequence of formation of the magnetic barrier which location corresponds to the maximum of the magnetic pressure (Fig. 2). The magnetic barrier is supported by the gas pressure of cold ionospheric plasma. This pressure is maintained by an ionization and ion chemical processes in the planetary upper atmosphere. At the bottom of the ionosphere, gas pressure is provided by the laying below neutral atmosphere through ion-neutral collisions.

The ionopause occurs at the place where the impacting solar wind pressure is balanced by the ionospheric pressure. From Fig. 2 it is seen that the dynamic pressure is negligibly

small downstream the bow shock as at the bow shock, the supersonic solar wind flow is diverted into a subsonic flow. Therefore, the ionopause is placed at the point where the gas pressure equals the magnetic pressure, at the distance about $0.04\ R_p \simeq 240$ km from the planetary surface. The altitude at which the ionopause is located is smallest at the nose, and it grows monotonically with increasing SZA, reaching the largest altitude at the terminator. The ionopause altitude is about $1\ R_p$ at the terminator [9].

Figure 3 shows the global configuration of the the magnetic field lines and plasma density from the final configuration of the numerical simulations. A view is from the tailside. The solar wind flows in from the left-hand side towards the planet. Brown lines indicate magnetic field lines which pile up at the bow shock, and then slip over the ionosphere, forming magnetotail. Magnetic field lines, after being dragged through the polar regions are convected equatorward by field line tension and solar wind flow toward the antisolar direction. The geometry of the magnetic field on the nightside is related to the draping of the solar wind magnetic field over the obstacle on the dayside. Some of the draped magnetic field apparently sinks into the wake of the planet to create lobes-like structures with sunward and anti-sunward directed magnetic field.
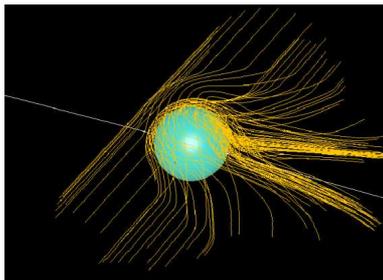


Fig. 3. Draping of magnetic field lines around Venus

## 4. Concluding remarks

This paper presents the Godunov-type scheme for two-component MHD equations. This scheme is accurate and efficient in its speed. It represents adequately complex flows and steep profiles, without generating spurious oscillations. This scheme is also *robust* as it has the virtue of giving reliable results to a wide range of problems without needing to be re-tuned. The developed numerical model of the solar wind interaction with the ionosphere of the planet Venus demonstrates the feasibility of fluid simulations in obtaining quantitative features in the magnetized fluid.

We considered the interaction of the solar wind with the ionosphere of Venus using numerical solutions of the two-component, three-dimensional MHD equations. For these solutions solar wind consists mainly of $H^+$ ions, while a primary component of the ionosphere consists of $O^+$ ions. Loss effects due to the interaction of $O^+$ ions with molecules of the carbon dioxide are introduced. Such modeling has generally been successful in reproducing characteristics of the solar wind interaction with Venus.

The main results are the following. The solar wind interaction with Venus leads to the formation of the bow shock

and the ionosphere which consists of cold, low speed, weakly magnetized $O^+$ ions. The ionosphere exhibits a blunt conic shape, with a highly structured ionotail. With a growing distance from the planetary surface, the ionotail is flattened and that flattening is believed to be due to magnetic field tension forces.

## REFERENCES

[1] E.R. Priest, *Solar Magnetohydrodynamics*, Reidel Publishing Company, Dordrecht, 1982.

[2] E. Toro, *Riemann Solvers and Numerical Methods for Fluid Dynamics*, Springer, Berlin, 2009.

[3] S.K. Godunov, "A difference scheme for numerical solution of discontinuous solution of hydrodynamic equations", *Math. Sb.* 47, 271–306 (1959).

[4] J.M. Stone and M.L. Norman, "ZEUS-2D: A radiation magnetohydrodynamics code for astrophysical flows in two space dimensions. I - The hydrodynamic algorithms and tests", *Astrophys. J. Suppl. Ser.* 80 (2), 753–790 (1992).

[5] K. Murawski and R.S. Steinolfson, "Numerical modeling of the solar wind interaction with Venus", *Planet. Space Sci.* 44, 243–252 (1996).

[6] P.R. Woodward and P. Colella, "The numerical simulation of two-dimensional fluid flow with strong shocks", *J. Comp. Phys.* 54, 115–173 (1984).

[7] P.L. Roe and D.S. Balsara, "Notes on the eigensystem of magnetohydrodynamics", *SIAM J. Appl. Math.* 56, 57–67 (1996).

[8] A.A. Barmin, A.G. Kulikovskiy, and N.V. Pogorelov, "Shock-capturing approach and non-evolutionary solutions in magnetohydrodynamics", *J. Comp. Phys.* 126 (1), 77–90 (1996).

[9] T Tanaka and K. Murawski, "Three dimensional MHD simulation of the solar wind interaction with the ionosphere of Venus: Results of two-component reacting plasma simulation", *J. Geophys. Res.* 102 (19), 805–819, 821 (1997).

[10] T. Tanaka, "Finite volume TVD scheme on an unstructured grid system for three-dimensional MHD simulation of inhomogeneous systems including strong background potential fields", *J. Comp. Phys.* 111 (2), 381–390 (1994).

[11] J.L. Phillips and D.J. McComas, "The magnetosheath and magnetotail of Venus", *Space Sci. Rev.* 55, 1–80 (1991).

[12] T.L. Zhang, J.G. Luhmann, and C.T. Russell, "The magnetic barrier at Venus", *J. Geophys. Res.* 96 (11), 145–153 (1991).

[13] K.K. Khurana and M.G. Kivelson, "A variable cross-section model of the bow shock of Venus", *J. Geophys. Res.* 99 (A5), 8505–8512 (1994).

[14] K.K. Mahajan, H.G. Mayr, L.H. Brace, and P.A. Cloutier, "On the lower altitude limit of the Venusian ionopause", *Geophys. Res. Lett.* 16, 759–762 (1989).

[15] L.H. Brace, W.T. Kasprzak, H.A. Taylor, R.F. Theis, C.T. Russell, A. Barnes, J.D. Mihalov, and D.M. Hunten, "The ionotail of Venus – its configuration and evidence for ion escape", *J. Geophys. Res.* 92, 15–26 (1987).

[16] T. Tanaka, "Effects of decreasing ionospheric pressure and the plasma mixing recess on the solar wind interaction with non-magnetized planets", *Adv. Space Res.* 26, 1577–1586 (2000).

[17] T.E. Cravens, A.J. Kliore, J.U. Kozyra, and A.F. Nagy, "The ionospheric peak on the Venus dayside", *J. Geophys. Res.* 86, 11323–11329 (1981).

[18] J.L. Phillips, J.G. Luhmann, and C.T. Russell, "Growth and maintenance of large-scale magnetic fields in the dayside Venus ionosphere", *J. Geophys. Res.* 89, 10676–10684 (1984).